In situ analysis of the tensile deformation mechanisms in extruded Mg–1Mn–1Nd (wt%)

C.J. Boehlert*[abc], Z. Chen[a], A. Chakkedath[a], I. Gutiérrez-Urrutia[d], J. Llorca[bc], J. Bohlen[e], S. Yi[e], D. Letzig[e] and M.T. Pérez-Prado[c]

An extruded Mg–1Mn–1Nd (wt%) (MN11) alloy was tested in tension in an SEM at temperatures of 323 K (50°C), 423 K (150°C), and 523 K (250°C) to analyse the local deformation mechanisms through *in situ* observations. Electron backscatter diffraction was performed before and after the deformation. It was found that the tensile strength decreased with increasing temperature, and the relative activity of different twinning and slip systems was quantified. At 323 K (50°C), extension twinning, basal, prismatic $\langle a \rangle$, and pyramidal $\langle c + a \rangle$ slip were active. Much less extension twinning was observed at 423 K (150°C), while basal slip and prismatic $\langle a \rangle$ slip were dominant and presented similar activities. At 523 K (250°C), twinning was not observed, and basal slip controlled the deformation.

1. Introduction

Lightweight magnesium (Mg) alloys are progressively being incorporated into commercial vehicles, where weight reduction and the corresponding fuel savings are important design priorities [1]. Most of the automobile parts currently being commercialised are fabricated by die casting, as the formability of wrought Mg alloys is limited due to the strong textures developed during processing. However, magnesium alloys containing rare earth (RE) elements exhibit weak rolling and extrusion textures, which endow them with a more isotropic mechanical behaviour and, therefore, better formability than conventional Mg alloys, such as the magnesium–zinc (AZ) series alloys [2–15]. Accordingly, these Mg–RE alloys are very promising light structural materials. However, the origin of the weak textures is still not known.

Recent studies have reported that the texture of Mg changes with increasing concentrations of different RE elements, namely lanthanum (La), yttrium (Y),

gadolinium (Gd), and cerium (Ce), following a common path [9]. For example, the extrusion texture of pure Mg (extrusion axis tilted 14° from the arc [10–10]–[11–20]) shifts first toward the extrusion texture of conventional alloys (extrusion axis perpendicular to the *c*-axes) with small RE contents and later to the so-called RE texture (extrusion axis aligned with the [10–10] and the [–12–11] directions) with larger RE contents. This change is generally accompanied by a decrease in the texture intensity. Another study found that neodymium (Nd) is a much stronger texture modifier than Ce or Y in extruded Mg–Mn alloys [11]. In rolled pure Mg, the *c*-axes are mostly aligned with the normal direction (ND) and slightly shifted toward the rolling direction (RD). The addition of RE elements results in an overall texture weakening, where a rolling texture develops in which the *c*-axes are shifted both toward the RD and transverse direction (TD) [2]. Again, the degree of texture weakening depends on the alloying element.

Several works have attempted to relate the development of weak wrought textures in Mg–RE alloys to the activation of deformation and recrystallisation mechanisms that are different to those of conventional Mg alloys [2–15]. In the latter, it is well known that the critical resolved shear stresses (CRSS) of the various slip and twinning systems vary at room temperature (RT) according to the following sequence: $CRSS_{basal} < CRSS_{\{10\ 12\}\ twinning} < CRSS_{prismatic} \leq CRSS_{pyramidal}$. Thus, basal slip and twinning are the preferred deformation mechanisms in randomly oriented polycrystals. As the temperature increases, the CRSS of non-basal systems decreases and the activity of these deformation modes increases gradually [16–22]. Grain boundary sliding (GBS) has also been observed, mostly at high temperatures and low strain rates. However, the deformation mechanisms operative in Mg–RE alloys are still not well understood. It has been reported that the activity of non-basal slip at low temperatures in Mg–RE alloys is enhanced, as compared with conventional Mg alloys, because the CRSS value of prismatic and pyramidal systems in Mg–RE alloys becomes closer to that of extension twinning and basal slip [3,4,12,14,15]. It has been hypothesised that the changes in the CRSS of the various slip systems might be attributed to the influence of RE solute elements on crystal structure features, such as the c/a ratio, the stacking fault energy, or the width of the dislocation cores. However, no clear experimental evidence of the deformation systems that are active under different testing conditions exists to date. Thus, there is a need to both quantify the relative activities of the different deformation modes present in Mg–RE alloys as a function of temperature and determine the CRSS values of the active slip systems.

The observations described above were extracted from *ex situ* experiments, in which the deformation and recrystallisation mechanisms are inferred from the observation of the microstructure before and after mechanical testing. Under these experimental conditions, it is not possible to determine the order of activation of the different deformation modes nor the stress or strain at which they occur during the experiment. In addition, the Schmid factors at which the various slip and twinning modes become operative cannot be estimated.

The aim of this work was to use *in situ* scanning electron microscopy (SEM) observations to investigate the deformation mechanisms that are active in an extruded Mg alloy containing neodymium (Mg–1Mn–1Nd (wt%)). This alloying element has been chosen owing to its potent texture weakening effect. Constant

strain rate tension experiments were performed along the extrusion direction at temperatures ranging from 323 K (50°C) to 523 K (250°C) to identify the onset of different slip and twinning systems as a function of temperature.

2. Experimental

2.1. *Material*

The MN11 material was gravity cast to produce a billet of original diameter equal to 125 mm. The billet was machined to a diameter of 93 mm in preparation for extrusion. The billet was homogenised at 623 K (350°C) for 15 h prior to extrusion. Indirect extrusion was carried out at 573 K (300°C) to produce a round bar with a diameter of 17 mm, which corresponds to an extrusion ration of 1:30. The extrusion rate was 5.6 mm/s which corresponded to a profile exit speed of 10 m/min. The as-extruded rod exhibited a weak texture. The bulk chemical composition of the as-extruded rod, measured using spark emission spectroscopy, was Mg–0.95Mn–0.94Nd–0.04Al–0.01Si–0.008Zn–0.007Ce (wt%).

Flat dog-bone samples were electrodischarge machined with the tensile axis parallel to the extrusion direction. One surface of the samples was mirror-polished. *In situ* tensile tests were performed at a constant displacement rate of 0.004 mm/s (equivalent to a strain rate of approximately $10^{-3}\,s^{-1}$) using a screw-driven tensile stage placed inside a Zeiss (Jena, Germany) EVO MA15 SEM. A minimum of two samples were tested at each of the following temperatures: 323 K (50°C), 423 K (150°C) and 523 K (250°C). Secondary electron (SE) SEM images were taken before loading and during interruptions at different displacements throughout the tensile test. Details of this apparatus and testing technique can be found elsewhere [23]. The microstructure in the center of the gage section was analysed before and after each tensile test by electron backscatter diffraction (EBSD) performed using a 6500 F JEOL field emission gun SEM equipped with a EDAX-TSL (Mahwah, NJ, USA) EBSD system. The grain size was calculated by the linear intercept method [24,25] in the EBSD orientation maps using only grain boundaries with misorientations greater than 15°. Following a previously described methodology [26], the active slip and twinning systems were identified using the EBSD data and the SE SEM images acquired during the tensile experiments.

3. Results

3.1. *Tension*

The as-extruded rod exhibited a weak texture, as reported previously [11], and similar weak textures have been observed in other Mg–RE alloys [9]. The average equiaxed grain diameter was approximately 5 μm. Representative stress versus displacement curves are plotted in Figure 1. Samples were not taken to failure to limit the deterioration of the sample surface so that EBSD orientation mapping could be performed after the test without further preparation. However, each specimen was deformed to a strain greater than 0.14. At 323 K (50°C), the yield stress (YS) was approximately 1.25 times that at 423 K (150°C), and approximately 1.43 times that at 523 K (250°C). The YS values were comparable to those found in the

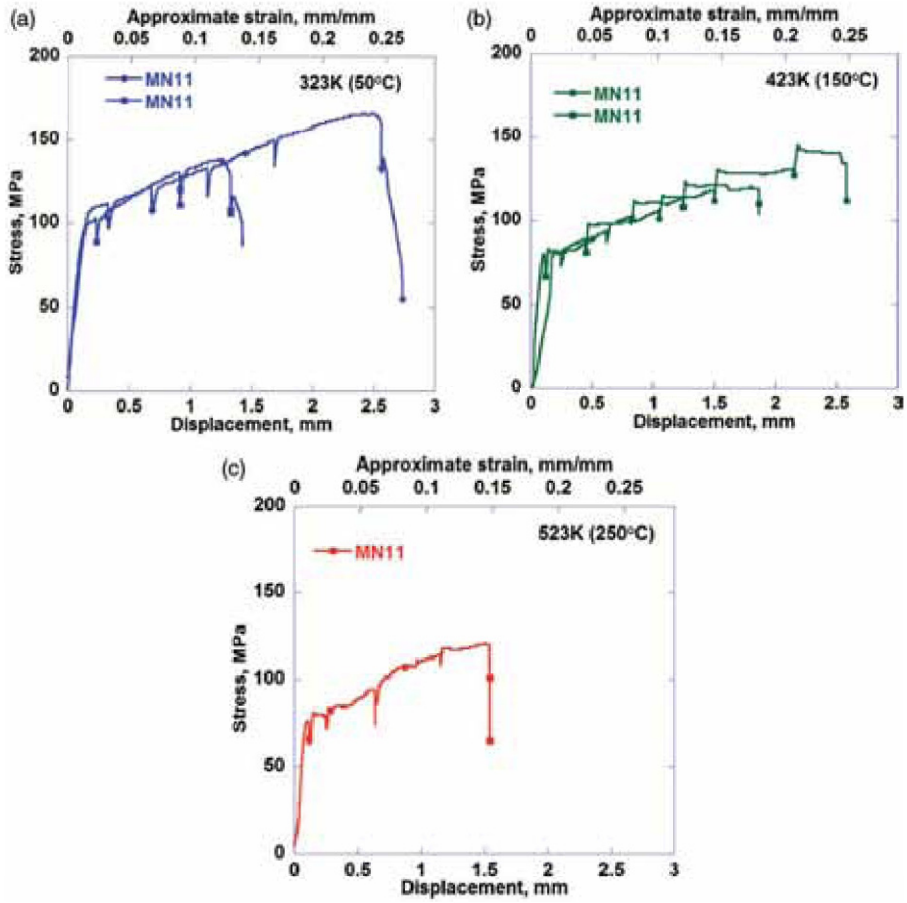

Figure 1. (colour online) Stress versus displacement plots for samples (a) 323 K (50°C), (b) 423 K (150°C), and (c) 523 K (250°C). The load-drops indicate the stress relaxation that occurred when the experiment was paused to acquire SE SEM photomicrographs.

literature for extruded MN11 [11]. The plastic anisotropy r values ($r = \varepsilon_w/\varepsilon_t$, where ε_ω and ε_t are the plastic strains in the sheet plane and along the thickness, respectively) were close to unity independent of temperature, indicating this alloy exhibited isotropic behavior, unlike that for wrought AZ31 which exhibits temperature-dependent r values between 2 and 4 [16,23,27–29].

The active slip and twinning systems were identified using the EBSD data and the SE SEM images acquired during the tensile experiments. Three slip modes and two twinning modes were considered in the analysis:

(1) $\{0\,0\,0\,1\}\langle -2\,1\,1\,0\rangle$: basal $\langle a\rangle$
(2) $\{0\,1\,-1\,0\}\langle 2\,-1\,-1\,0\rangle$: first order prism $\langle a\rangle$
(3) $\{1\,1\,-2\,2\}\langle -1\,-1\,2\,3\rangle$: second order pyramidal $\langle c+a\rangle$
(4) $\{1\,0\,-1\,2\}\langle -1\,0\,1\,1\rangle$: extension twin
(5) $\{1\,0\,-1\,1\}\langle 1\,0\,-1\,-2\rangle$: contraction twin.

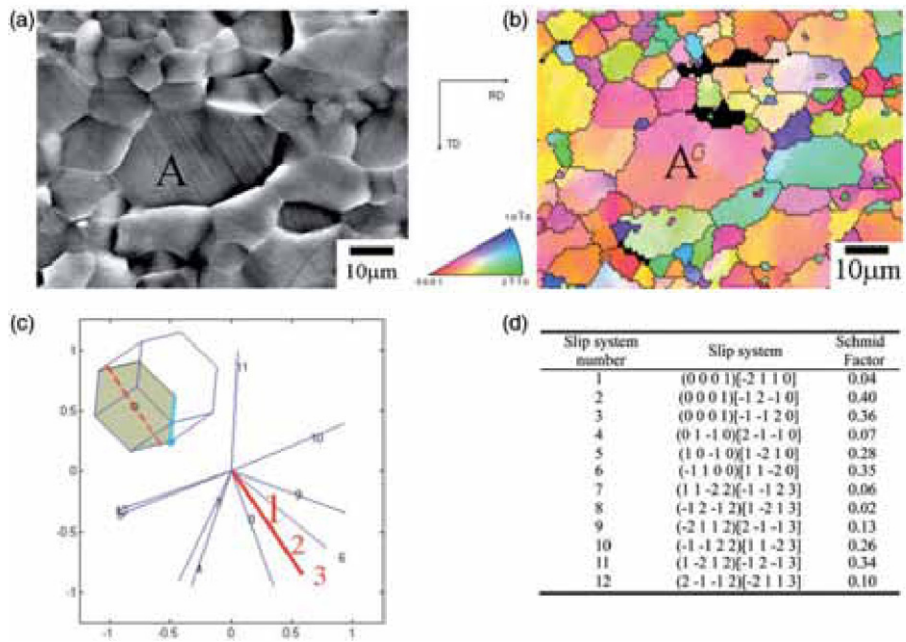

Slip system number	Slip system	Schmid Factor
1	(0 0 0 1)[-2 1 1 0]	0.04
2	(0 0 0 1)[-1 2 -1 0]	0.40
3	(0 0 0 1)[-1 -1 2 0]	0.36
4	(0 1 -1 0)[2 -1 -1 0]	0.07
5	(1 0 -1 0)[1 -2 1 0]	0.28
6	(-1 1 0 0)[1 1 -2 0]	0.35
7	(1 1 -2 2)[-1 -1 2 3]	0.06
8	(-1 2 -1 2)[1 -2 1 3]	0.02
9	(-2 1 1 2)[2 -1 -1 3]	0.13
10	(-1 -1 2 2)[1 1 -2 3]	0.26
11	(1 -2 1 2)[-1 2 -1 3]	0.34
12	(2 -1 -1 2)[-2 1 1 3]	0.10

Figure 2. Examples of the slip trace analysis performed for grain A for a sample tested at 523 K (250°C). (a) SE SEM image taken at 67 MPa, at ~14.5% strain. (b) EBSD orientation maps in the ND. (c) Slip system selection; note that 2 was the selected system based on the match and this corresponds to the (0 0 0 1) plane and [−2 1 1 0] direction. The unit cell of hcp Mg with the slip trace was indicated by the red dotted line and the Burgers vector was indicated by the light blue line starting from the solid circle is shown in the inset. (d) The Schmid factors for the slip systems in (c).

Figure 2 illustrates examples of the procedure used to identify the active slip systems based on the slip trace analysis. This approach makes use of SE SEM images and EBSD orientation data input into a MATLAB code.

3.1.1. *Tensile tests at T = 323 K (50°C)*

Figure 1a illustrates the stress-displacement curves for the two samples tested at 323 K (50°C) along the extrusion direction. The average YS was approximately 100 MPa. Figure 3 shows the EBSD inverse pole figure (IPF) maps along ND and the corresponding pole figures for the same area of the sample before and after the test. The RD and TD in the pole figure corresponded to the extrusion and radial directions of the sample, respectively. The noticeable colour gradients within grains on the EBSD map were indicative of large plastic deformation. As inferred from the pole figures, the specimen exhibited a weak texture before the test, with a slight alignment of the pyramidal directions with the extrusion axis. This texture was retained during deformation.

Figure 4 shows SE SEM images of the same region taken at different strains, in the range 3.5–29.4%, during the tensile tests. Bright particles were aligned as stringers in the extrusion direction, indicating that the cast billet was inhomogeneous

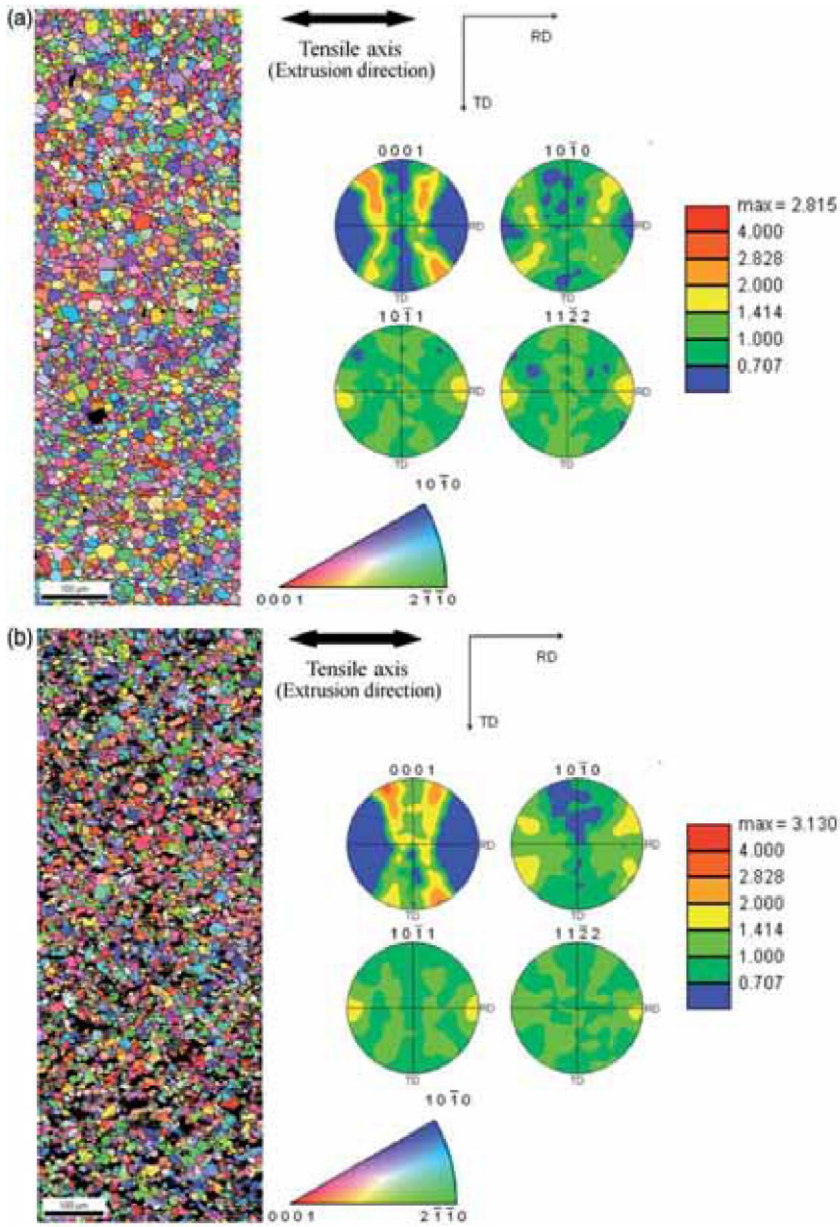

Figure 3. (colour online) EBSD inverse pole figure maps in the ND for a sample tested at 323 K (50°C) along the extrusion direction (a) before testing and (b) after ~29.4% tensile strain. The corresponding pole figures are also included.

with respect to the alloying elements. Energy dispersive spectroscopy (EDS) analysis showed that these second-phase particles were enriched in Nd content. Due to the low volume fraction of these second-phase particles, we considered that their effect on the deformation mechanisms was negligible.

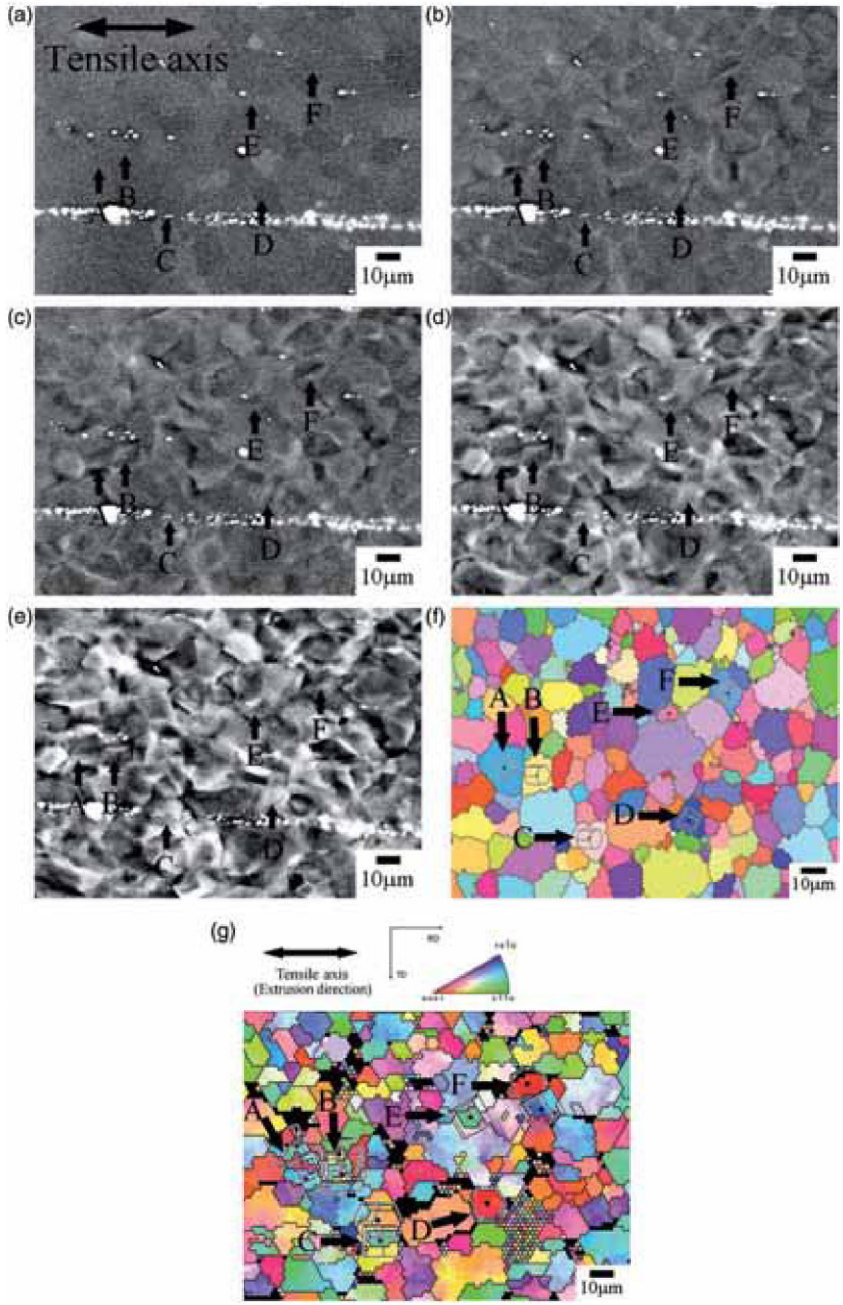

Figure 4. (colour online) SE SEM photomicrographs for a sample tested at 323 K (50°C) along the extrusion direction, corresponding to a displacement of (a) 0.47 mm (~3.5% strain), (b) 0.65 mm (~5.3% strain), (c) 1.01 mm (~8.9% strain) and (d) 2.02 mm (~19.0% strain), (e) 3.06 mm (~29.4% strain), (f) EBSD inverse pole figure map in the ND before testing, and (g) EBSD inverse pole figure in the ND after testing. Twinning was observed in the grains labelled A–F in the figures when the applied strain was greater than 3.5%.

Combining the SEM and EBSD observations, the active deformation modes were identified. Twinning was observed at the early stages of deformation (95–112 MPa/ 3.5–5.3% strain). Slip traces were observed after the sample reached approximately 9% strain. Deformation twins were found in several grains, referred as A, B, C, D, E, and F in Figure 4. For grains A, B, D, and F, twinning was first observed at approximately 5.3% strain (Figure 4b). As the deformation proceeded, the twin area fraction increased, and twinning ultimately consumed a large part of the parent grain. Figure 4 also shows the EBSD IPF map along ND of this region both before (Figure 4f) and after (Figure 4g) the tensile test. The reorientation of the grains due to twinning is indicated by the unit cell drawn on the map. For grains C and E, the twinned region is not clear on the SEM image, but can be identified on the IPF map. The orientation relationship between the reoriented grain and the parent grain ranged between 84.5 and 89.5° about the $\langle 1\,1\,-2\,0\rangle$ direction. This suggests the formation of the $\{-1\,1\,0\,2\}\langle 1\,-1\,0\,1\rangle$ extension twin which ideally reorients the lattice 86.3° about the $\langle 1\,1\,-2\,0\rangle$ direction. No contraction twins were identified within the region of observation.

The active deformation modes were determined for 29 slip traces and 13 twins in different grains. Figure 5 summarises the Schmid factor distribution for the deformation modes observed in samples tested at 323 K (50°C). Among the 29 slip traces analysed, 21 were basal $\langle a\rangle$ slip, two were first order prismatic $\langle a\rangle$ slip, and six were second order pyramidal $\langle c+a\rangle$ slip. The Schmid factor distribution for pyramidal $\langle c+a\rangle$ slip system was wider than that for the other two slip systems.

3.1.2. *Tensile tests at $T = 423$ K (150°C)*

Figure 1b illustrates the stress–displacement curves corresponding to the two tensile tests performed along the extrusion direction at 423 K (150°C). The average YS was

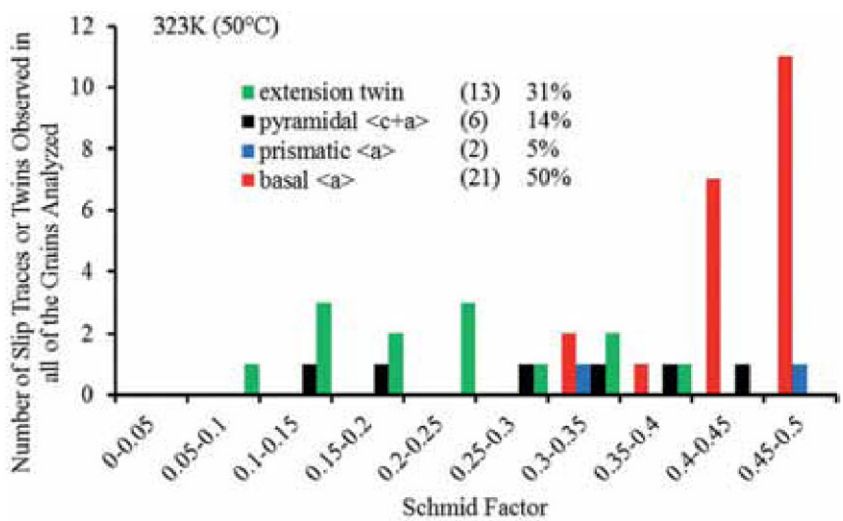

Figure 5. (colour online) Schmid factor distributions of the observed deformation modes for samples tensile tested at 323 K (50°C).

approximately 80 MPa. Figure 6 shows the EBSD inverse pole figure maps along ND and the corresponding pole figures for the same area of the sample both before and after the test. The specimen exhibited a weak texture before the test, which was maintained after the tensile deformation, following the pattern observed at 323 K (50°C).

As was found at 323 K (50°C), extension twinning was observed at 423 K (150°C) during the early stages of deformation (81–94 MPa/1.3–5.0% strain). The relative amount of twinning was significantly lower than that observed at 323 K (50°C). No contraction twins were found. Figure 7 shows the SE SEM photomicrographs of the same area of a sample before testing (Figure 7a) and deformed to different strain levels, 9.3% (Figure 7b), 20.3% (Figure 7c), and 24.6% (Figure 7d). Slip traces were

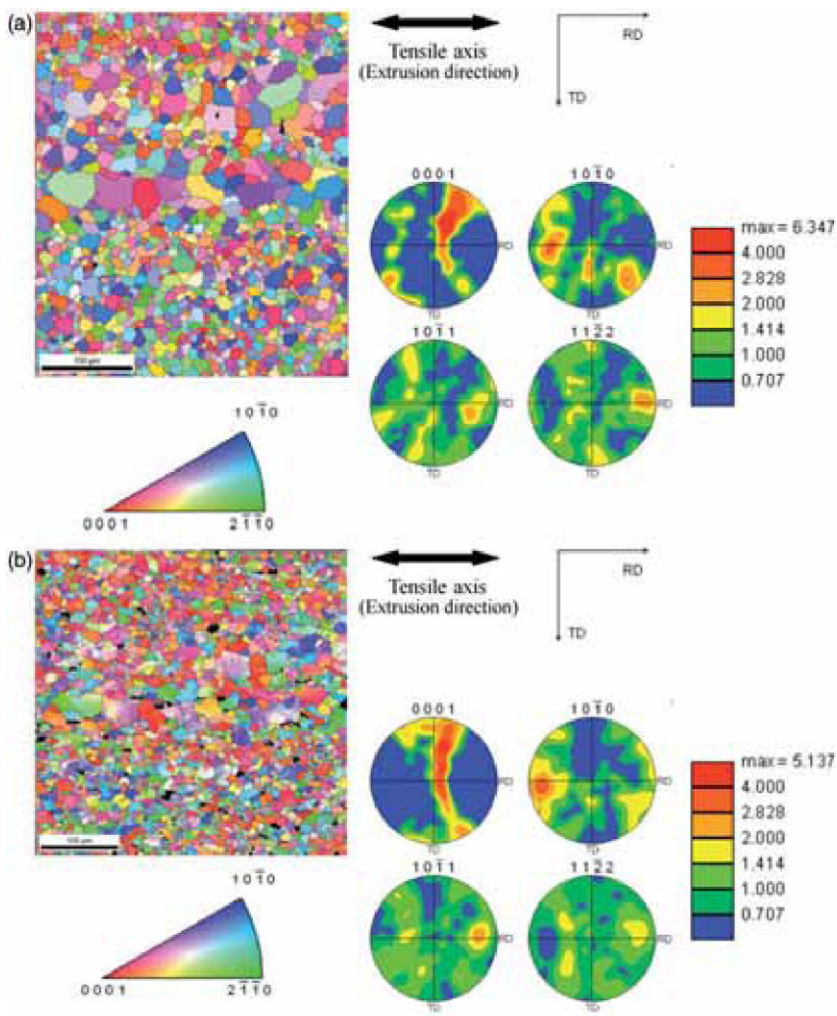

Figure 6. (colour online) EBSD inverse pole figure maps in the ND for a sample tested at 423 K (150°C) along the extrusion direction (a) before testing and (b) after ~24.6% tensile strain. The corresponding pole figures are also included.

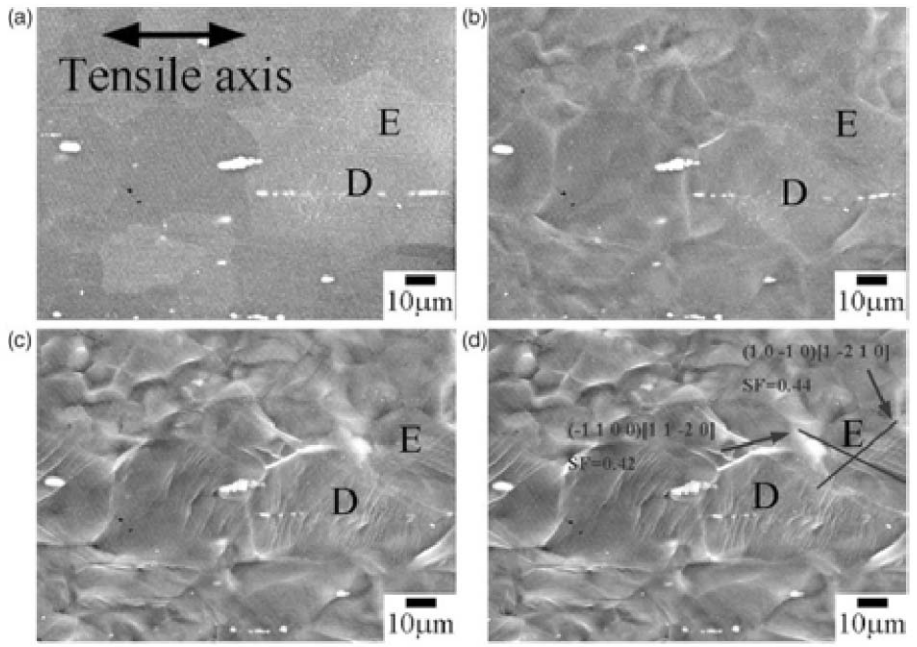

Figure 7. SE SEM photomicrographs of a sample tested at 423 K (150°C) along the extrusion direction; the approximate strain values were (a) 0%, (b) 9.3%, (c) 20.3%, and (d) 24.6%. The Schmid factor and the predicted trace direction for the most likely slip systems calculated from the EBSD data are also labelled in (d).

first observed between approximately 5.0 and 9.3% strain. An increase in the density of slip traces can be clearly observed with increasing strain in Figure 7a–d. Grain D represents an example in which the slip trace became wavy as the deformation increased. This suggests the activation of dislocation cross-slip. In some other grains, wavy slip traces were also observed. However, the slip trace direction was generally not clear enough due to the severe deformation of the sample, so the corresponding slip systems were not identified. In a few grains, slip traces for two slip systems with different Burgers vectors were observed. For instance, grain E contained two sets of slip traces corresponding to first order prismatic $\langle a \rangle$ slip; (1 0 −1 0)[1 −2 1 0] and (−1 1 0 0)[1 1 −2 0].

In the samples tested at 423 K (150°C), the active deformation modes were determined for 46 different slip traces and three twins. Figure 8 summarises the Schmid factor distribution and stress levels at which slip traces were observed for each slip system in these samples. Among the 46 slip traces analysed, 29 were basal $\langle a \rangle$ slip, 14 were prismatic $\langle a \rangle$ slip, and three were second order pyramidal $\langle c+a \rangle$ slip, see Figure 8. Most slip occurred with Schmid factors greater than 0.4.

3.1.3. *Tensile tests at $T = 523$ K (250°C)*

A representative stress–strain curve corresponding to a tensile test performed along the extrusion direction at 523 K (250°C) is plotted in Figure 1c. The average

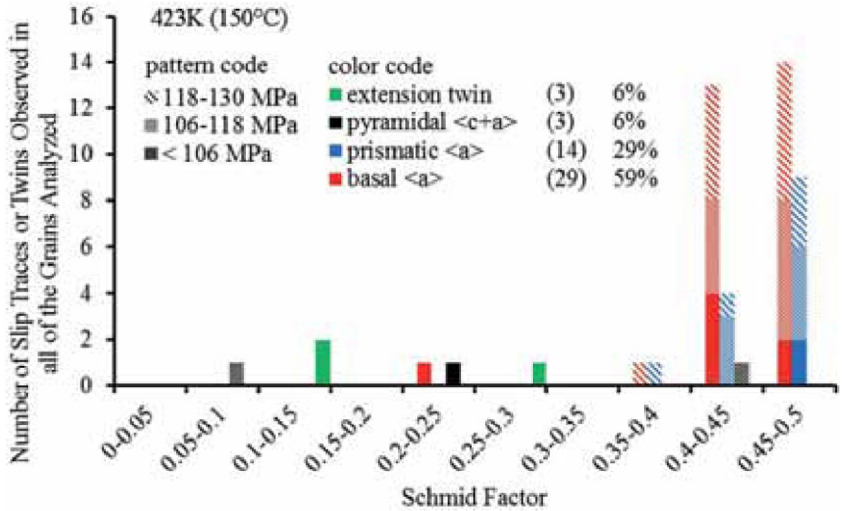

Figure 8. (colour online) Schmid factor distributions and stress levels at which twinning and slip traces were observed for each of the deformation modes for samples tensile tested at 423 K (150°C).

YS was 70 MPa. Figure 9 shows the EBSD inverse pole figure maps along ND. This specimen exhibited a weak texture after the tensile deformation.

In the samples tested at 523 K (250°C), the slip traces and grain boundaries were more obvious than in the samples tested at lower temperatures. Figure 10 shows SE SEM photomicrographs of the same area of a sample tested at 523 K (250°C) to different strain levels, (a) 0%, (b) 1.3%, (c) 5.2%, and (d) 24.0%. Some grain boundary ledges could be distinguished after about 1.3% strain, as shown in Figure 10b, while slip traces were first observed at approximately 1.3–5.2% strain. Some slip traces were wavy-type, such as in grain A in Figure 10d.

The slip systems were determined for 55 slip traces in the samples tested at 523 K (250°C); 48 were basal $\langle a \rangle$ slip, one was prismatic $\langle a \rangle$ slip, and six were second order pyramidal $\langle c + a \rangle$ slip. This indicates that basal $\langle a \rangle$ slip was the dominant deformation mode at high temperatures. Figure 11 depicts the distribution of the Schmid factors for each of the slip traces observed and the corresponding stress levels. The Schmid factors for the active slip systems in the samples tested at 523 K (250°C) were distributed over a range comparable to the specimens tested at 423 K (150°C).

4. Discussion

Recent literature has summarised the CRSS values in both single crystals and polycrystals of pure Mg and Mg alloys at RT [30,31]. From the review by Hutchinson and Barnett [31], one would expect very low CRSS values for basal $\langle a \rangle$ slip; on the order of ~1 MPa [32–34]. However, for the harder prismatic $\langle a \rangle$ slip, the values for CRSS ranged between 39 and 50 MPa [35,36]. Due to the hardening process that takes place in polycystals, the values expected for basal $\langle a \rangle$ slip increase

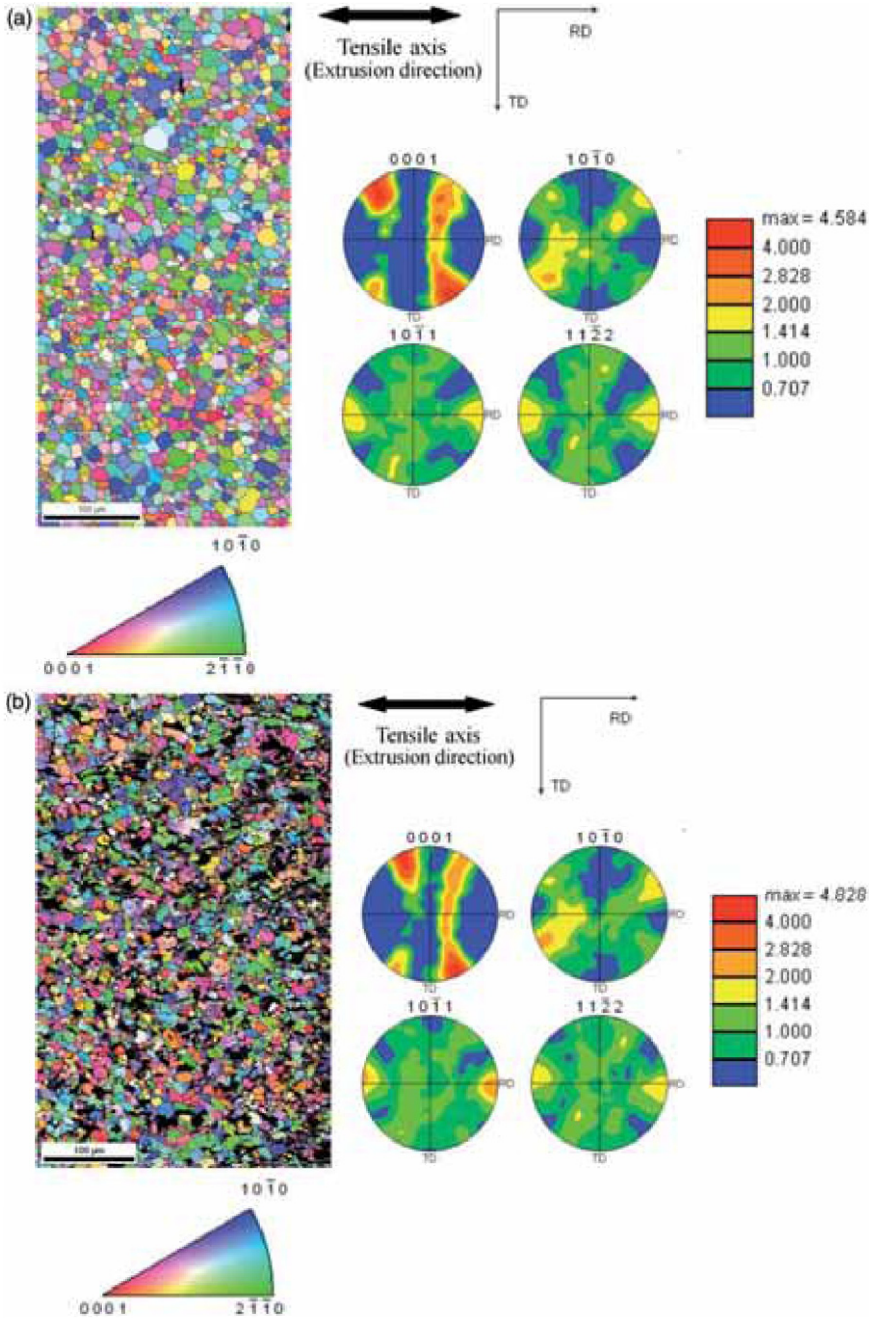

Figure 9. (colour online) EBSD inverse pole figure maps in the ND for a sample tested at 523 K (250°C) along the extrusion direction (a) before testing and (b) after ~24.0% tensile strain. The corresponding pole figures are also included.

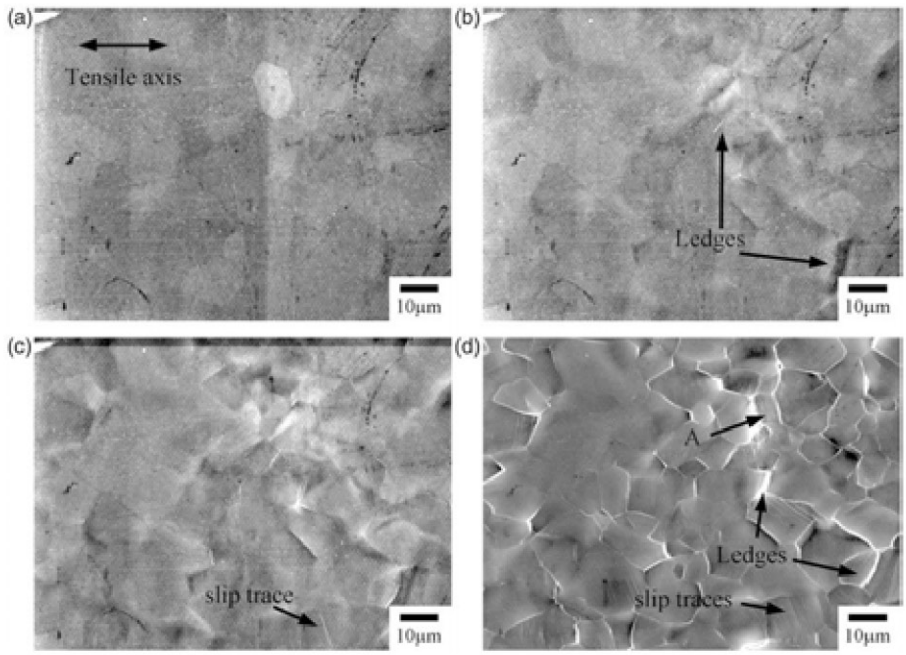

Figure 10. SE SEM photomicrographs for a sample tested at 523 K (250°C) along the extrusion direction. The approximate strain values were (a) 0%, (b) 1.3%, (c) 5.2%, and (d) 24.0% strain. The arrows point to ledges and slip traces.

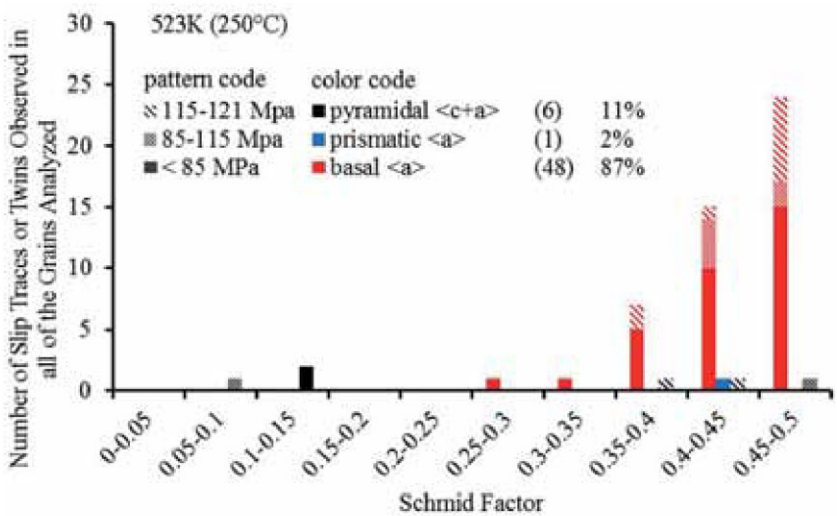

Figure 11. (colour online) Schmid factor distributions and stress levels at which the slip trace was observed for each of the slip systems for samples tensile tested at 523 K (250°C).

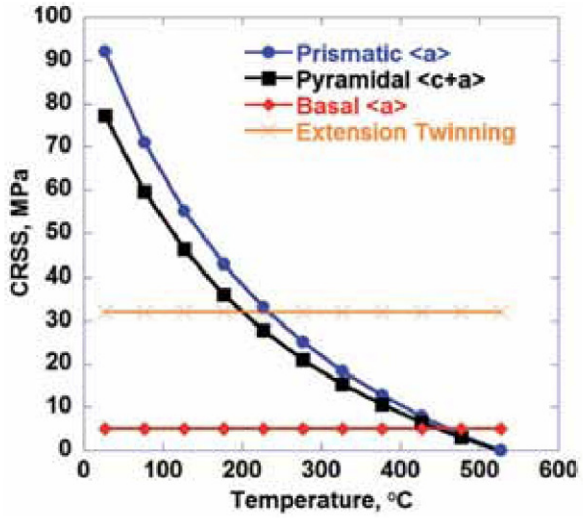

Figure 12. (colour online) Variation of the CRSS of prismatic $\langle a \rangle$ and pyramidal $\langle c+a \rangle$ slip with temperature in an extruded AZ31 polycrystalline microstructure according to the equations provided in [20].

to 10–50 MPa [19,37–39], and the corresponding prism $\langle a \rangle$ CRSS values increase to between 55 and 110 MPa [19,37–39]. Thus, there is a significant discrepancy in the literature in the CRSS values between single crystals and polycrystals at RT. The hardening process in polycrystals could be treated as an additional term of similar magnitude to the CRSS values of the different slip systems, leading to the reduction of the ratio between the CRSS of non-basal and basal slip system in polycrystals compared to single crystals. Raeisinia et al. [30] suggest that by incorporating the effect of grain size and solute concentration on individual deformation modes into their polycrystal modelling, the difference between the CRSS values determined from single crystal experiments and polycrystal modelling can be reconciled.

The variation with temperature of the CRSS of the various slip and twinning systems active in Mg alloys has been estimated by crystal plasticity models in polycrystals and also via experiments in single crystals. We will begin by discussing polycrystalline results. Barnett [20] used a full constraint Taylor model to estimate the evolution of the CRSS for prismatic $\langle a \rangle$ and pyramidal $\langle c+a \rangle$ slip in an extruded AZ31 alloy at temperatures ranging from 423 to 723 K (150–450°C). He assumed the temperature-independent values of CRSS for basal slip and extension twinning to be 5 and 32 MPa, respectively. Figure 12 illustrates the output of this model and predicts that the CRSS of prismatic $\langle a \rangle$ slip is higher than that of pyramidal $\langle c+a \rangle$ slip within the temperature range 323–773 K (50–500°C). The CRSS of prismatic and pyramidal slip are smaller than that of twinning above 506 K (233°C) and 473 K (200°C), respectively. The CRSS of non-basal systems has been reported to be higher than that of basal slip until temperatures close to 733 K (460°C) [20]. The results obtained from single crystal experiments are the following. Chapuis and Driver [40] measured the CRSS of basal, prismatic $\langle a \rangle$ slip and pyramidal $\langle c+a \rangle$ slip, as well as of various twinning systems, at temperatures ranging from 573 to 723 K

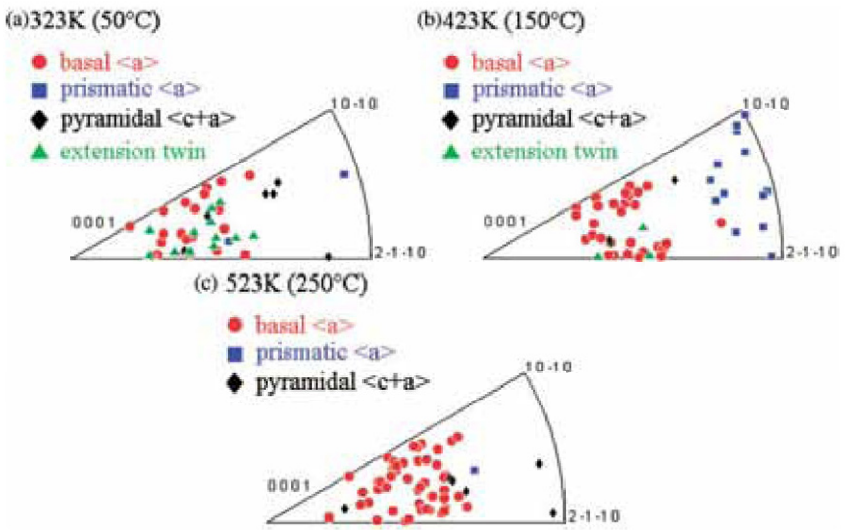

Figure 13. (colour online) Inverse pole figures of the tensile direction (extrusion direction) for grains in which different deformation modes were observed at (a) 323 K (50°C), (b) 423 K (150°C), and (c) 523 K (250°C).

(300–450°C). They reported that the CRSS of basal slip and extension twinning were basically temperature independent in the range 298–723 K (25–450°C) with approximate values of 3 and 7–10 MPa, respectively. They also found that the CRSS of pyramidal slip was higher than that of prismatic sip within the temperature range investigated and that neither of them became comparable to that of extension twinning until 723 K (450°C). Thus, there is also a significant discrepancy in the literature between the CRSS values between single crystals and polycrystals at elevated temperature.

Our *in situ* experiments provide new insight on the deformation mechanisms of Mg–RE alloys. The relative contributions of the different deformation modes at 323 K (50°C) were 31% extension twin, 50% basal, 5% prismatic $\langle a \rangle$, and 14% pyramidal $\langle c+a \rangle$. The relative contributions of the different deformation modes at 423 K (150°C) were 6% extension twin, 59% basal, 29% prismatic $\langle a \rangle$, and 6% pyramidal $\langle c+a \rangle$. The relative contributions of the different slip systems at 523 K (250°C) were 87% basal, 2% prismatic $\langle a \rangle$, and 11% pyramidal $\langle c+a \rangle$. Thus, it appeared that the activity of basal and non-basal slip is more balanced at lower temperatures compared to higher temperatures, at which basal slip was more dominant. Figure 13 shows the inverse pole figures (IPF) of the tensile direction (extrusion direction) for grains in which different deformation modes were observed. The tensile direction of most of the grains in which basal slip or extension twinning was identified lies in the middle part of the IPF for all three different temperatures at which experiments were performed. Most of the grains in which prismatic $\langle a \rangle$ slip was identified had the tensile direction lie near the arc of the IPF, which is similar to observations made for AZ31 elsewhere [39]. There was a larger variation in the tensile direction for grains in which pyramidal $\langle c+a \rangle$ slip was found. Thus, the higher percentage of prismatic $\langle a \rangle$ slip observed at 423 K (150°C) might be related to the fact

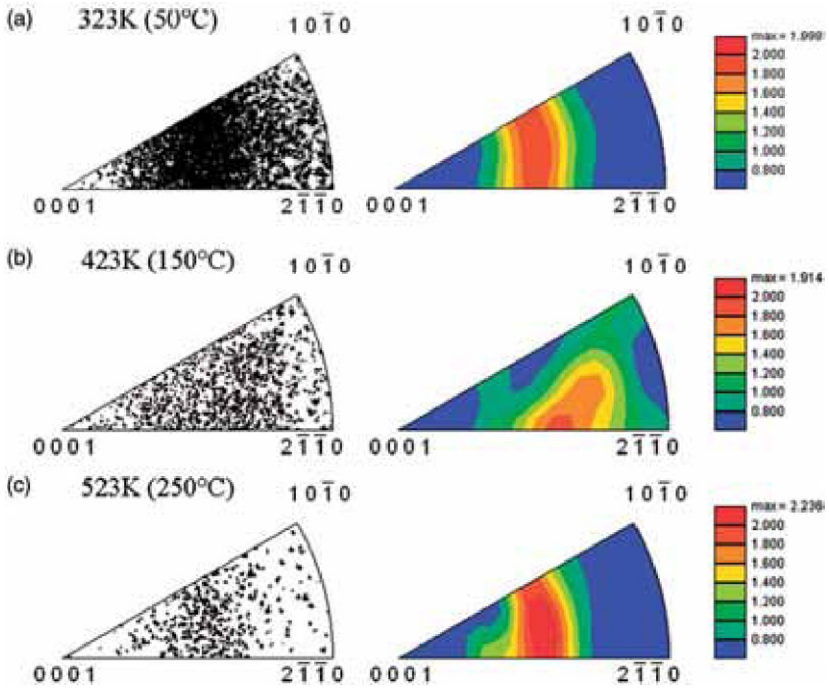

Figure 14. (colour online) Discrete inverse pole figures and inverse pole figures of the tensile direction for regions in which the *in situ* SEM images were taken for deformation mode analysis for samples tested at (a) 323 K (50°C), (b) 423 K (150°C), and (c) 523 K (250°C).

that more grains in which prismatic $\langle a \rangle$ slip was favourable were taken into account in the analysis.

This is supported by Figure 14, which shows the discrete inverse pole and inverse pole figures of the tensile direction for regions in which the *in situ* SEM images were taken for the deformation mode analysis. For the 423 K (150°C) tested sample, the tensile direction was distributed more uniformly on the IPF compared to samples tested at the other two temperatures. In other words, the region analysed at 423 K (150°C) had a different local orientation distribution compared to those regions analysed at the other two temperatures. Thus, a direct comparison of the percentage of the different modes operating at the different temperatures may not be completely fair. Therefore, a smaller area was cropped from the original region within which the deformation mode analysis was performed. This smaller area showed a more similar local orientation distribution as the regions analysed under the other two temperatures (Figure 15a). Figure 15b shows the inverse pole figure of the tensile direction for grains in which different deformations activities were observed at 150°C, with only grains within this cropped area being considered. This results in the percentage of basal slip increasing from 50 to 75 to 87% with increasing temperature from 323 K (50°C) to 423 K (150°C) to 523 K (250°C), respectively. Twinning decreases from 31 to 3 to 0% with increasing temperature from 323 K (50°C) to 423 K (150°C) to 523 K (250°C), respectively. The prismatic slip and pyramidal

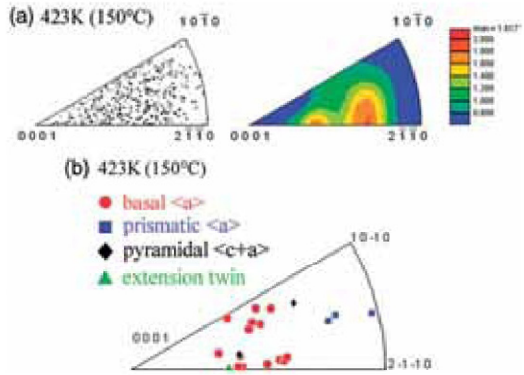

Figure 15. (colour online) (a) Discrete inverse pole figures and inverse pole figures of the tensile direction for an area cropped from the regions in which the *in situ* SEM images were taken for deformation mode analysis for the 423 K (150°C) tested sample. (b) Inverse pole figure of the tensile direction (extrusion direction) for grains in which different deformation modes were observed, with only grains within the cropped area being considered.

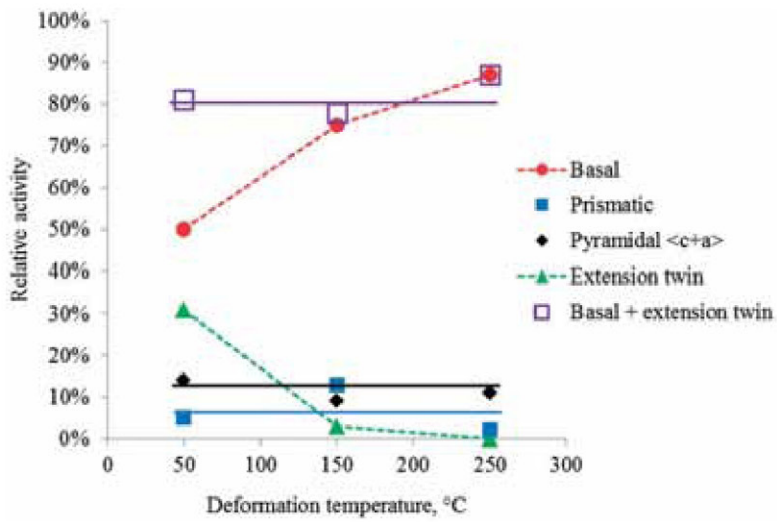

Figure 16. (colour online) Plot depicting the percentages of each deformation mode with respect to temperature after taking into account the differences in the grain orientations in the regions analysed for the three different deformation temperatures. In other words, the data points in Figure 15b were used instead of data points in Figure 13b.

$\langle c+a \rangle$ slip system percentages do not change markedly with temperature. Upon grouping the twin and basal slip systems, the percentage of these "soft" modes remains basically the same for all three of the deformation temperatures analysed. Essentially, the strain accommodated by twins is replaced by basal slip at the higher temperatures.

Taking this analysis into account, Figure 16 shows the percentages of each deformation mode with respect to temperature, and this plot illustrates that basal slip replaces twinning at elevated temperatures. Overall, the results suggest that the activation of basal slip compared to non-basal slip and twinning is easier at higher temperatures and that the relative activity of twinning is reduced significantly with increasing temperature.

At 323 K (50°C), the CRSS of basal slip and twinning for MN11 seems to be quite close since both are active to similar extents. However, at higher temperatures, deformation in MN11 takes place mainly by basal slip and this mechanism was active even in grains in which the Schmid factor was very low. Conversely, the relative activity of non-basal slip remained relative constant (i.e. between ~10 and 20% for all the temperatures analysed when taking into account the grain orientation analysis mentioned in the above paragraph), and prismatic slip traces occurred in grains in which the corresponding Schmid factor was high. Although we were not able to determine the CRSS values for the deformation modes in the polycrystalline microstructure examined, the present study reveals that, in the MN11 alloy, the CRSS of basal slip appears to decrease with temperature. This result is different to that obtained in conventional Mg alloys, such as AZ31, where the CRSS values is expected to remain constant. We propose that as temperature increases, RE-atom diffusion takes place more readily and thus dislocation movement along basal planes becomes increasingly easier. If the temperature is high enough, it is likely that the CRSS of basal slip in the MN11 alloy might tend to that of pure Mg and more conventional Mg alloys not containing RE elements. Extension twinning was prevalent at 323 K (50°C), but its intensity decreased at 423 K (150°C) and it was not observed at 523 K (250°C). This suggests that the CRSS of both basal and non-basal slip become lower than that of extension twinning at a temperature around 423 K (150°C). This transition temperature is slightly higher than that observed in an AZ31 alloy [32] and slightly lower than that predicted by Figure 12.

At 323 K (50°C), the YS in MN11 (YS~100 MPa) was lower than that for a AZ31 rolled sheet tensile tested along RD (YS~150 MPa), when prismatic slip dominates [23]. This agrees with the expected higher CRSS for prismatic slip compared to basal slip at lower temperatures. It is noteworthy, however, that at elevated temperatures, the strength of the MN11 alloy is greater than that for AZ31. For example, at 423 K (150°C), the YS and UTS in MN11 was approximately 80 and 150 MPa, respectively, while the YS and UTS in AZ31 was approximately 90 and 120 MPa, respectively [23]. At 523 K (250°C), the YS and UTS in MN11 was approximately 70 and 125 MPa, respectively, while the YS and UTS in AZ31 was approximately 50 and 60 MPa, respectively [23]. Thus, the rare earth addition, which is expected to be responsible for this elevated-temperature strengthening through both solid-solution strengthening and precipitation strengthening [41], is more dominant than the texture effects at elevated temperatures. In addition, an increase in the CRSS of basal slip may be expected in the MN11 alloy compared to the AZ31 alloy if the preferential location of RE atoms is along the basal planes. Future work is planned to model the deformation behaviour of the MN11 and AZ31 systems and estimate the CRSS values of the different deformation modes as a function of temperature.

5. Summary and conclusions

Extruded MN11 samples were tested in tension in an SEM at temperatures of 323 K (50°C), 423 K (150°C), and 523 K (250°C), and SE SEM images were acquired during the deformation. EBSD orientation maps were acquired both before and after deformation on the same local microstructural patch. The following conclusions can be drawn from the present study:

(1) The relative slip activity between the basal and prismatic and pyramidal slip systems was quantified. At 323 K (50°C), extension twinning, basal $\langle a \rangle$, prismatic $\langle a \rangle$, and pyramidal $\langle c+a \rangle$ slip were active. At 423 K (150°C), much less extension twinning was observed. At 523 K (250°C), twinning was not observed, and basal slip controlled the deformation.
(2) Taking into account the different grain orientations involved in the analysis for the samples deformed at 423 K (150°C), the prismatic slip and pyramidal $\langle c+a \rangle$ slip system percentages did not change markedly with temperature and the percentage of the combined basal slip + twinning modes remained basically the same for all three of the deformation temperatures. Therefore, the strain accommodated by twinning at the lower temperatures was replaced by basal slip at the higher temperatures.
(3) The CRSS of basal slip is believed to decrease with increasing temperature for MN11.

Acknowledgements

This work was supported by the National Science Foundation Division of Material Research (Grant No. DMR1107117) and by the Spanish Ministry of Science and Innovation (grants PRI-PIBUS-2011-990 and PRI-PIBUS-2011-917) through the Materials World Network program. CJB acknowledges the support from the Spanish Ministry of Education for his sabbatical period in Madrid (SAB2009-0045). The authors would also like to thank the vehicle interior manufacturer, Grupo Antolin Ingeniería, S.A., within the framework of the project MAGNO2008-1028-CENIT funded by the Spanish Ministry of Science and Innovation. The authors acknowledge Professors Thomas Bieler and Martin Crimp of Michigan State University for their prior work in developing the slip trace analysis technique.

References

[1] M. Bamberger and G. Dehm, Annu. Rev. Mater. Res. 38 (2008) p.505.
[2] J. Bohlen, M.R. Nurnberg, J.W. Senn, D. Letzig and S.R. Agnew, Acta Mater. 55 (2007) p.2101.
[3] Y. Chino, M. Kado and M. Mabuchi, Acta Mater. 56 (2008) p.387.
[4] Y. Chino, M. Kado and M. Mabuchi, Mater. Sci. Eng. A 494 (2008) p.343.
[5] R.K. Mishra, A.K. Gupta, P.R. Rao, A.K. Sachdev, A.M. Kumar and A.A. Luo, Scripta Mater. 59 (2008) p.562.
[6] L.W.F. Mackenzie and M.O. Pekguleryuz, Scripta Mater. 59 (2008) p.665.
[7] R. Cottam, J. Robson, G. Lorimer and B. Davis, Mater. Sci. Eng. A 485 (2008) p.375.
[8] N. Stanford, D. Atwell, A. Beer, C. Davies and M.R. Barnett, Scripta Mater. 59 (2008) p.772.
[9] N. Stanford, Mater. Sci. Eng. A 527 (2010) p.2669.

[10] N. Stanford, D. Atwell and M.R. Barnett, Acta Mater. 58 (2010) p.6773.
[11] J. Bohlen, S.B. Yi, D. Letzig and K.U. Kainer, Mater. Sci. Eng. A 527 (2010) p.7092.
[12] S. Sandlobes, S. Zaefferer, I. Schestakow, S. Yi and R. Gonzalez-Martinez, Acta Mater. 59 (2011) p.429.
[13] L. Jiang, J.J. Jonas and R. Mishra, Mater. Sci. Eng. A 528 (2011) p.6596.
[14] J.D. Robson, A.M. Twier, G.W. Lorimer and P. Rogers, Mater. Sci. Eng. A 528 (2011) p.7247.
[15] T. Al-Samman and X. Li, Mater. Sci. Eng. A 528 (2011) p.3809.
[16] S.R. Agnew and O. Duygulu, Int. J. Plast. 21 (2005) p.1161.
[17] G.Y. Chin and W.L. Mammel, Metall. Trans. 1 (1970) p.357.
[18] S.R. Agnew, M.H. Yoo and C.N. Tome, Acta Mater. 49 (2001) p.4277.
[19] S.R. Agnew, C.N. Tome, D.W. Brown, T.M. Holden and S.C. Vogel, Scripta Mater. 48 (2003) p.1003.
[20] M.R. Barnett, Metall. Mater. Trans. A 34A (2003) p.1799.
[21] X.Y. Lou, M. Li, R.K. Boger, S.R. Agnew and R.H. Wagoner, Int. J. Plast. 23 (2007) p.44.
[22] I. Ulacia, N.V. Dudamell, F. Galvez, S. Yi, M.T. Perez-Prado and I. Hurtado, Acta Mater. 58 (2010) p.2988.
[23] C.J. Boehlert, Z. Chen, I. Gutierrez-Urrutia, J. Llorca and M.T. Perez-Prado, Acta Mater. 60 (2012) p.1889.
[24] Standard Test Methods for Determining Average Grain Size, ASTM E112-96E3, ASTM International, West Conshohocken, PA, 2004.
[25] J.E. Hilliard, Met. Prog. 84 (1964) p.99.
[26] C.J. Boehlert, H. Li, L. Wang and B. Bartha, Adv. Mater. Process 168 (2010) p.41.
[27] N. Stanford, K. Sotoudeh and P.S. Bate, Acta Mater. 59 (2011) p.4866.
[28] B. Hutchinson, M.R. Barnett, A. Ghaderi, P. Cizek and I. Sabirov, Int. J. Mater. Res. 100 (2009) p.556.
[29] M.R. Barnett, A. Ghaderi, I. Sabirov and B. Hutchinson, Scripta Mater. 61 (2009) p.277.
[30] B. Raeisinia, S.R. Agnew and A. Akhtar, Metall. Trans. A 42 (2011) p.1418.
[31] W.B. Hutchinson and M.R. Barnett, Scripta Mater. 63 (2010) p.737.
[32] E. Schmid, Z. Elektrochem. 37 (1931) p.447.
[33] P.W. Bakarian and C.H. Mathewson, Trans. Am. Inst. Min. Metall. Eng. 152 (1943) p.226.
[34] H. Conrad and W.D. Robertson, Trans. Am. Inst. Min. Metall. Eng. 209 (1957) p.503.
[35] R.E. Reed-Hill and W.D. Robertson, Trans. Am. Inst. Min. Metall. Eng. 209 (1957) p.496.
[36] P. Ward Flynn, J. Mote and J.E. Dorn, Trans. Metall. Soc. AIME 221 (1961) p.1148.
[37] S.R. Agnew, D.W. Brown and C.N. Tome, Acta Mater. 54 (2006) p.4841.
[38] O. Muránsky, D.G. Carr, M.R. Barnett, E.C. Oliver and P. Šittner, Mater. Sci. Eng. A 496 (2008) p.14.
[39] M.R. Barnett, Z. Keshavarz and X. Ma, Metall. Mater. Trans. A 37A (2006) p.2283.
[40] A. Chapuis and J.H. Driver, Acta Mater. 59 (2011) p.1986.
[41] L.L. Rokhlin, *Magnesium Alloys Containing Rare Earth Metals: Structure and Properties*, Taylor & Francis, London, 2003.